Matter and Radiation at Extremes | RESEARCH ARTICLE | scitation.org/journal/mre

Hybrid fluid–particle modeling of shock-driven hydrodynamic instabilities in a plasma

Cite as: Matter Radiat. Extremes 6, 035901 (2021); doi: 10.1063/5.0042973
Submitted: 5 January 2021 • Accepted: 1 March 2021 •
Published Online: 22 March 2021

View Online Export Citation CrossMark

Hong-bo Cai,[1,2,a)] Xin-xin Yan,[3] Pei-lin Yao,[4] and Shao-ping Zhu[1,5,6,b)]

AFFILIATIONS

[1]Institute of Applied Physics and Computational Mathematics, Beijing 100094, China
[2]Center for Applied Physics and Technology, HEDPS, and College of Engineering, Peking University, Beijing 100871, China
[3]Center for Applied Physics and Technology, HEDPS, School of Physics, and College of Engineering, Peking University, Beijing 100871, China
[4]Department of Engineering Physics, Tsinghua University, Beijing 100084, China
[5]Graduate School, China Academy of Engineering Physics, P.O. Box 2101, Beijing 100088, China
[6]Science and Technology on Plasma Physics Laboratory, Laser Fusion Research Center, CAEP, 621900 Mianyang, China

Note: This paper is part of the Special Issue on Progress in Matter and Radiation at Extremes in China.
a)Author to whom correspondence should be addressed: cai_hongbo@iapcm.ac.cn
b)Electronic mail: zhu_shaoping@iapcm.ac.cn

ABSTRACT

Shock-driven hydrodynamic instabilities in a plasma usually lead to interfacial mixing and the generation of electromagnetic fields, which are nonequilibrium processes coupling kinetics with meso- and macroscopic dynamics. The understanding and modeling of these physical processes are very challenging tasks for single-fluid hydrodynamic codes. This work presents a new framework that incorporates both kinetics and hydrodynamics to simulate shock waves and hydrodynamic instabilities in high-density plasmas. In this hybrid code, ions are modeled using the standard particle-in-cell method together with a Monte Carlo description of collisions while electrons are modeled as a massless fluid, with the electron heat flux and fluid–particle energy exchange being considered in the electron pressure equation. In high-density plasmas, Maxwell's equations are solved using Ohm's law instead of Ampère's law. This hybrid algorithm retains ion kinetic effects and their consequences for plasma interpenetration, shock wave propagation, and hydrodynamic instability. Furthermore, we investigate the shock-induced (or gravity-induced) turbulent mixing between a light and a heavy plasma, where hydrodynamic instabilities are initiated by a shock wave (or gravity). This study reveals that self-generated electromagnetic fields play a role in the formation of baroclinic vorticity along the interface and in late-time mixing of the plasmas. Our results confirm the ability of the proposed method to describe shock-driven hydrodynamic instabilities in a plasma, in particular, nonequilibrium processes that involve mixing and electromagnetic fields at the interface.

I. INTRODUCTION

In inertial confinement fusion (ICF),[1] understanding and suppressing shock-driven hydrodynamic instabilities[2,3] and the ion mix[4,5] are crucial for achieving ignition. In a plasma, the evolution of both shock wave and hydrodynamic instabilities depends on the ion–ion mean free path (MFP), $\lambda_{ii} = 1/\sigma n_i$, where n_i is the ion density and σ is the collisional cross-section. In high-density and low-temperature plasmas, where the ion–ion MFP is much smaller than the gradient scale length $L = (d \log n_i/dx)^{-1}$ of the plasma, i.e., $\lambda_{ii} \ll L$, the system is entirely dominated by collisions and can be described satisfactorily by hydrodynamic simulations. In the opposite regime, $\lambda_{ii} \gg L$, the shock wave is collisionless, and the system is usually treated kinetically using, for example, particle-in-cell (PIC) methods. However, a difficult task is faced when attempting to handle the physics in the transition regime with $\lambda_{ii} \simeq L$, where ion kinetic processes usually play an important role, and therefore a hydrodynamic description of such moderate-density plasmas is no longer valid.

Several regions inside ICF hohlraums have been found where kinetic plasma effects are expected to play an important role. For instance, for shock wave propagation at the inner surface of the capsule[6] and in the rebound of the shock wave from the center,[7] laser/plasma interactions during the laser drive,[8] and plasma interpenetration at the

hohlraum wall/gas interface,[9,10] the standard single-fluid descriptions are inadequate. Furthermore, fully kinetic simulation methods, such as standard PIC and Fokker–Planck codes, are computationally expensive because they need to resolve the plasma frequency $\omega_{pe} = \sqrt{4\pi n_e e^2/m_e}$.[11]

In these regimes, electromagnetic hybrid fluid–PIC codes (in which ions are treated as particles and electrons as constituting a massless fluid) are more reliable and adaptable tools for investigating such complex kinetic plasma behavior. This hybrid approach is valid because the simulation time is much longer than the relaxation time of electron–electron collisions and the simulated plasma scale is much larger than the Debye length of the plasma. Furthermore, the hybrid fluid–PIC method has many merits: (i) The ions are modeled kinetically, with the possibility of handling non-Maxwellian ion distributions, which allows the hybrid method to intrinsically capture many effects that are difficult or impossible for fluid simulations. (ii) The hybrid method does not have to resolve the electron spatial scale, i.e., the Debye length, and the associated time scale. Therefore, modeling much larger spatial/temporal scales than can be dealt with using a fully kinetic method[12] becomes possible. (iii) The influence of self-generated magnetic fields, which can result from misaligned density and temperature gradients $\nabla n_e \times \nabla T_e$,[13] can be included.

In the last few years, hybrid fluid–PIC techniques have emerged as an efficient solution to nonequilibrium plasma simulations of, for example, high-Mach-number shock waves,[14] laser–plasma interactions and hot-electron generation,[15] magnetized pinches,[16] plasma interpenetration,[17] species separation,[18] high-energy particle transport,[19–24] and fast ignition physics.[25,26] Furthermore, electromagnetic hybrid plasma codes have been developed to study collisionless shocks[27] and Kelvin–Helmholtz instability[12] in collisionless plasmas. However, most of these codes use the Darwin approximation and thus exclude completely the propagation of electromagnetic waves.

In this article, we first present a new approach using the hybrid fluid–PIC technique to provide a more accurate estimation of the complex late-time behavior of shock-driven hydrodynamic instabilities. An important distinction between this approach and that adopted in the models considered by Davies *et al.*,[20] Xu *et al.*,[22] and Honrubia and Meyer-ter-Vehn[24] is that we retain a particle description for all the ions in the plasma. Furthermore, our approach is distinguished from the models considered by Lembege and Simonet,[27] Thoma *et al.*,[15] Higginson *et al.*,[17] and Cohen *et al.*[25] in that we use the density continuity equation and retain the displacement current in Ampère's law (i.e., we do not apply the Darwin approximation) to make sure that charge conservation is satisfied and the charge separation electric field is also simultaneously included throughout the simulation.

We then present a fundamental study of shock-driven instabilities, which indicates that hydrodynamic instabilities could be more harmful to ICF than predicted by hydrodynamic simulations: the increased ion mix can enhance thermal energy loss and reduce the implosion performance in ICF, and the distortion of the transmitted shock wave may affect shock convergence in the ICF implosion. This should provide motivation for future studies of shock-driven hydrodynamic instabilities under more realistic plasma conditions.

II. ALGORITHMS FOR HYBRID FLUID–PIC SIMULATION CODE

Here, the kinetic PIC and fluid models are combined in a single hybrid code Ascent-H (where "Ascent" stands for Assembly System for Computational ExperimeNT), which incorporates a Monte Carlo binary collision model, the PIC method, and fluid techniques. The model allows us to assess the complex late-time behavior of shock waves and shock-driven hydrodynamic instabilities. While the ion dynamics are treated kinetically using standard PIC techniques, the electrons are modeled as a massless fluid. Ascent-H also provides the capability for evaluating self-generated electromagnetic fields and small-scale structure hydrodynamic instabilities, which can substantially increase interfacial growth compared with the hydrodynamic case.

The hybrid model is based upon our previously developed relativistic electromagnetic PIC code Ascent-P.[28] In the following subsections, we provide the details of the newly developed methodology for calculating electron fluid current, electron pressure, electric field, magnetic field, and the collisional force between the electron fluid and the ions.

A. Deviation of Ohm's law for electric field

The equations of motion for electrons and ions in a plasma can be written as follows:[29]

$$n_i m_i \frac{d\mathbf{V}_i}{dt} = eZ_i n_i \left(\mathbf{E} + \mathbf{V}_i \times \frac{\mathbf{B}}{c}\right) - \nabla p_i - \nabla \cdot \pi_i + \mathbf{R}, \tag{1}$$

$$n_e m_e \frac{d\mathbf{V}_e}{dt} = -en_e \left(\mathbf{E} + \mathbf{V}_e \times \frac{\mathbf{B}}{c}\right) - \nabla p_e - \nabla \cdot \pi_e - \mathbf{R}, \tag{2}$$

where $\boldsymbol{\pi}_j$ $(j = e, i)$ is the anisotropic viscosity tensor, which gives rise to stresses within each fluid. Here, the terms $\nabla \cdot \boldsymbol{\pi}_j$ will be ignored, since the associated collisions do not give rise to much diffusion. The term $\mathbf{R} = \mathbf{R}_u + \mathbf{R}_T$ represents the transfer of momentum between electrons and ions by collisions. It consists of two parts: (i) a frictional force $\mathbf{R}_u$, which is due to the existence of a relative velocity $\mathbf{u} = \mathbf{V}_e - \mathbf{V}_i$, with $\mathbf{V}_e = -\mathbf{J}_e/en_e$, and (ii) a thermal force $\mathbf{R}_T$ due to the gradient in the electron temperature. These frictional and thermal forces are given by[30]

$$\mathbf{R}_u = -\alpha_\parallel \mathbf{u}_\parallel - \alpha_\perp \mathbf{u}_\perp + \alpha_\wedge (\mathbf{b} \times \mathbf{u}), \tag{3}$$

$$\mathbf{R}_T = -\beta_\parallel^{uT} \nabla_\parallel T_e - \beta_\perp^{uT} \nabla_\perp T_e - \beta_\wedge^{uT} (\mathbf{b} \times \nabla T_e), \tag{4}$$

respectively, where

$$\alpha_\parallel = \alpha_0 \eta, \qquad \alpha_\perp = \eta \left(1 - \frac{\alpha_1' \chi^2 + \alpha_0'}{\Delta}\right),$$

$$\alpha_\wedge = \eta \frac{\chi}{\Delta} (\alpha_1'' \chi^2 + \alpha_0''),$$

$$\beta_\parallel^{uT} = n_e \beta_0, \qquad \beta_\perp^{uT} = n_e \frac{\beta_1' \chi^2 + \beta_0'}{\Delta},$$

$$\beta_\wedge^{uT} = n_e \frac{\chi (\beta_1'' \chi^2 + \beta_0'')}{\Delta},$$

η is the resistivity, and $\boldsymbol{b} = \boldsymbol{B}/|\boldsymbol{B}|$ is the unit vector in the direction of the magnetic field. The subscripts $\parallel$ and $\perp$ on the vectors denote the components respectively parallel and perpendicular to the magnetic field; for example, $\boldsymbol{u}_\parallel = \boldsymbol{b}(\boldsymbol{b} \cdot \mathbf{u})$ and $\boldsymbol{u}_\perp = \boldsymbol{b} \times (\boldsymbol{u} \times \boldsymbol{b})$. The values of the

parameters α_0, α_0', α_1', α_0'', α_1'' and β_0, β_0', β_1', β_0'', β_1'' are given in Refs. 30,31.

Note that the Hall parameter $\chi = \omega_{ce}\tau_e$ is an important quantity here. It compares the electron magnetization parameter ω_{ce} with the electron collision time τ_e, which determines how the magnetic field inhibits the electron thermal conduction. The cyclotron frequency for the electrons is

$$\omega_{ce} = eB/m_e c = 1.76\times10^7 B \quad \mathrm{rad/s}. \tag{5}$$

The electron collision time is

$$\tau_e = \frac{3\sqrt{m_e}\,T_e^{3/2}}{4\sqrt{2\pi}\,Z^2e^4 n_i \ln\Lambda} = 3.44\times10^5\frac{T_e^{3/2}}{n_e\ln\Lambda} \quad \mathrm{s}, \tag{6}$$

where $\ln\Lambda$ is the Coulomb logarithm. Note that the Coulomb logarithm, electron collision time, and resistivity can also be given by the Lee–More model.[32] In solid-density plasmas, plasma waves will be damped out, since the collision frequency ($\sim n_e$) is higher than the plasma frequency ($\sim \sqrt{n_e}$). In this case, electron inertia is no longer important. Therefore, we can derive a generalized Ohm's law as follows. We multiply Eq. (1) by eZ_i/m_i and sum over ion species i. We then add the resulting equation to Eq. (2) multiplied by $-e/m_e$. Taking the limit as $m_e/M_i \to 0$, we obtain the generalized Ohm's law

$$\mathbf{E} + \mathbf{V}\times\frac{\mathbf{B}}{c} = \eta_\parallel\mathbf{J}_\parallel + \eta_\perp\mathbf{J}_\perp - \frac{1}{en_e}\left(\nabla p_e - \mathbf{R} - \mathbf{J}\times\frac{\mathbf{B}}{c}\right), \tag{7}$$

which provides an explicit, algebraic determination of the electric field.

In Eq. (7), $\mathbf{V} \simeq (m_i\mathbf{V}_i + m_e\mathbf{V}_e)/(m_i + m_e)$ is the mass velocity and $\mathbf{J} \equiv e\,(n_i\mathbf{V}_i - n_e\mathbf{V}_e)$ is the total current density, where $\mathbf{V}_e = -\mathbf{J}_e/n_e$ is the background electron velocity. ∇p_e is the gradient of the electron pressure. In our high-density hybrid model, we use a scalar pressure $p_e = n_e kT_e$, although this can easily be generalized to a tensor pressure. Note that the $\mathbf{V}\times\mathbf{B}/c$ term and the Hall term $\mathbf{J}\times\mathbf{B}/c$ in Eq. (7) can be neglected in the case of unmagnetized and/or weakly magnetized plasmas. However, when a significant magnetic field is present, the frictional force of the ions on the electrons leads to a tensor resistivity

$$\eta = \eta_\parallel\mathbf{bb} + \eta_\perp(\mathbf{I} - \mathbf{bb}) - \eta_\wedge(\mathbf{b}\times). \tag{8}$$

Note that when the Hall parameter $\chi \ll 1$, $\eta_\parallel\mathbf{J}_\parallel + \eta_\perp\mathbf{J}_\perp$ can be simplified to $\eta\mathbf{J}$, where the resistivity η can be calculated using the Spitzer model[33] or the Lee–More model.[32] To avoid numerical problems at shock fronts in simulations, it is sometimes useful to include a small amount of artificial viscosity in Eq. (7). As is well known, the viscosity arises from particle–particle collisions, which convert fluid velocity into thermal energy. In our hybrid fluid–PIC code, the ion–ion collisions and ion–electron collisions are handled self-consistently. Therefore, an artificial viscosity is not necessary. In the hybrid code, the electron pressure gradient term ∇p_e, the momentum transfer term $\mathbf{R}_T + \mathbf{R}_u$, and the Hall term $\mathbf{J}\times\mathbf{B}$ in Eq. (7) can be considered or not depending on the setting of the control parameters.

Once we have the electric field, the magnetic field can be obtained through Faraday's law

$$\frac{\partial\mathbf{B}}{\partial t} = -c\nabla\times\mathbf{E}. \tag{9}$$

On substituting Eq. (7) into Eq. (9), we obtain an equation for the self-generated magnetic field

$$\frac{\partial\mathbf{B}}{\partial t} = \nabla\times(\mathbf{V}\times\mathbf{B}) - \nabla\times\left(\frac{\mathbf{J}}{en_e}\times\mathbf{B}\right) + c\nabla\times\left(\frac{\nabla p_e}{en_e}\right) - c\nabla\times\left(\frac{\mathbf{R_T} + \mathbf{R}_u}{en_e}\right) - c\nabla\times\left(\eta_\parallel\mathbf{J}_\parallel + \eta_\perp\mathbf{J}_\perp\right). \tag{10}$$

The first term on the right-hand side of this equation corresponds to frozen-in advection of the magnetic field. The second term is the Hall term, which causes the magnetic field to advect at a velocity $\mathbf{V} - \mathbf{J}/en_e \simeq (m_i\mathbf{V}_i + m_e\mathbf{V}_e)/(m_i + m_e) - (\mathbf{V}_i - \mathbf{V}_e) \simeq \mathbf{V}_e$, since $m_i \gg m_e$. The third term $c\nabla\times(\nabla p_e/en_e)$ is the Biermann battery term, which is usually the main source of self-generated magnetic fields.[13] The fourth term slows down advection of the magnetic field into the hot region. The fifth term is the resistive diffusion term. Thus, our hybrid fluid–PIC code includes the source term, resistive dissipation, and advection of the self-generated magnetic field due to both the plasma flow and the Nernst term. Note that in the case of shock-driven hydrodynamic instability, the thermal and flow pressures usually dominate the magnetic pressure, i.e., the plasma beta parameter $\beta = 8\pi p/B^2 \gg 1$. This means that although such magnetic fields do not affect the hydrodynamics directly, they do have an indirect effect on the plasma conditions by altering the electron heat transport.[34]

B. Equations for electron fluid current and density

The electron fluid current can be calculated using Ampère's law

$$\mathbf{J}_e = \frac{c}{4\pi}\nabla\times\mathbf{B} - \frac{1}{4\pi}\frac{\partial\mathbf{E}}{\partial t} - (\mathbf{J}_i + \mathbf{J}_p), \tag{11}$$

where $\mathbf{J}_i$ is the total current of the background ions and $\mathbf{J}_p$ is the total current of injected particle beams. Usually, we have $\mathbf{J}_p \simeq 0$ for the case without an injected beam. In some cases, the displacement current $\partial\mathbf{E}/\partial t$ can be neglected, which means that plasma oscillations at ω_{pe} will be neglected. In our hybrid fluid–PIC model, the displacement current is retained. That is to say, charge separation effects can also be simultaneously included. If we apply the continuity equation

$$\frac{\partial\rho}{\partial t} + \nabla\cdot\mathbf{J} = 0, \tag{12}$$

where $\mathbf{J} = \mathbf{J}_e + \mathbf{J}_i + \mathbf{J}_p$ is the total current and ρ is the charge density, we can see that Eq. (11) implies that the Poisson equation $\nabla\cdot\mathbf{E} = 4\pi\rho$ is satisfied rigorously, which means that charge conservation holds throughout the simulation. Equation (11) can be used to obtain the electron number density n_e, since $\rho = -e(n_e - Zn_i)$.

C. Electron fluid pressure equation

In the present model, the electron fluid pressure $p_e = n_e kT_e$ is used. Therefore, the electron temperature can be obtained from the electron fluid pressure equation[35]

$$\left(\frac{\partial}{\partial t} + \mathbf{V}_e\cdot\nabla\right)p_e = -\gamma P_e\nabla\cdot\mathbf{V}_e - \nabla\cdot\mathbf{q}_e + Q_e, \tag{13}$$

where the terms on the right-hand side are the "PdV" term, the electron heat flux, and the electron heating, respectively. The electron heat flux $\mathbf{q}_e = \mathbf{q}_e^u + \mathbf{q}_e^T$ consists of two analogous parts,

$$\mathbf{q}_e^u = \beta_\parallel^{Tu}\mathbf{u}_\parallel + \beta_\perp^{Tu}\mathbf{u}_\perp + \beta_\wedge^{Tu}(\mathbf{b}\times\mathbf{u}), \tag{14}$$

$$\mathbf{q}_e^T = -\kappa_\parallel^e \nabla_\parallel T_e + \kappa_\perp^e \nabla_\perp T_e + \kappa_\wedge^e (\mathbf{b}\times\nabla T_e), \tag{15}$$

where

$$\beta_\parallel^{Tu} = \beta_\parallel^{uT} T_e, \qquad \beta_\perp^{Tu} = \beta_\perp^{uT} T_e, \qquad \beta_\wedge^{Tu} = \beta_\wedge^{uT} T_e,$$

$$\kappa_\parallel^e = \frac{n_e T_e \tau_e}{m_e}\gamma_0, \qquad \kappa_\perp^e = \frac{n_e T_e \tau_e}{m_e}\frac{(\gamma_1' x^2 + \gamma_0')}{\Delta},$$

$$\kappa_\wedge^e = \frac{n_e T_e \tau_e}{m_e}\frac{x(\gamma_1'' x^2 + \gamma_0'')}{\Delta}.$$

The values of the parameters γ_0, γ_0', γ_1', γ_0'', and γ_1'' are given in Ref. 30.

The electron heat flux due to collisions with ions is given by

$$Q_e = -(\mathbf{R}_u + \mathbf{R}_T)\cdot\mathbf{u} - Q_i, \tag{16}$$

where $\mathbf{R}_u$ and $\mathbf{R}_T$ are defined in Eqs. (3) and (4), and the ion heating Q_i is given by

$$Q_i = \sum_j \frac{3m_e}{m_j}\frac{Z^2 n_j}{\tau_e}(T_e - T_j). \tag{17}$$

Note that the scale length of the electron temperature gradient can become comparable to or even shorter than the thermal electron MFP. In such cases, the classical thermal conduction in $\nabla\cdot\mathbf{q}_e$ can result in inaccurate or even unphysical results. Note that $\kappa_\parallel^e$, $\kappa_\perp^e$, and $\kappa_\wedge^e$ are usually different in the presence of a magnetic field, which means that electron heat transport is affected by the magnetic field. Furthermore, the diffusive thermal flux $\mathbf{q}_e^T$ can even exceed the free-streaming value $v_{\rm th} n_e k T_e$ in regions with a large temperature gradient ∇T_e. A common way to handle these problems is to use a flux limiter, i.e., limit the electron thermal flux to be less than the value $f_e v_{\rm th} n_e k T_e$, where f_e is the so-called flux limiter. Here, a flux limiter value of $f_e = 0.03$–0.1 is used in the simulations with a flux-limited thermal transport model.

D. Ion motion and electron–ion momentum transfer

In our hybrid fluid–PIC model, the ions are dealt with by the standard PIC method. For an ion particle with position $\mathbf{x}_i$ and charge q_i, the equation of motion can be derived from Eq. (1) as

$$m_i\frac{d\mathbf{v}_i}{dt} = q_i\left(\mathbf{E} + \mathbf{v}_i\times\frac{\mathbf{B}}{c}\right) + \mathbf{F}_{ie}(\mathbf{x}_i) - n_i m_i \sum_{j=1}^{N_j} \nu_{ij}(\mathbf{v}_i - \mathbf{v}_j). \tag{18}$$

The electromagnetic fields and the collision force in this equation, needed at the ion position $\mathbf{x}_i$, are evaluated from the cell-vertex (nodal) values using a fifth-order conservative weighting scheme. The electromagnetic fields at the nodes are evaluated using Eqs. (7) and (10). The term $n_i m_i \sum_{j=1}^{N_j} \nu_{ij}(\mathbf{v}_i - \mathbf{v}_j)$ corresponds to ion–ion collisions, which can be handled by a binary collision model with the Monte Carlo method.[36] Ion–electron collisions are incorporated into the PIC method through the collision force at the nodes, which is given by Jones *et al.*[37] as

$$\mathbf{F}_{ie} = \nu_{ie} m_{ie}(\langle\mathbf{v}_e\rangle - \langle\mathbf{v}_i\rangle) + \left[\frac{\nu_{ie}^\varepsilon (T_i - T_e)}{\langle\mathbf{v}_i^2\rangle - \langle\mathbf{v}_i\rangle^2} - \frac{\nu_{ie} m_{ie}^2 (\langle\mathbf{v}_e\rangle - \langle\mathbf{v}_i\rangle)^2}{m_i(\langle\mathbf{v}_i^2\rangle - \langle\mathbf{v}_i\rangle^2)}\right](\langle\mathbf{v}_i\rangle - \mathbf{v}_i), \tag{19}$$

where the angle brackets $\langle\rangle$ indicate averaging over the species distribution function, and $m_{ie} = m_i m_e/(m_i + m_e)$ is the reduced mass. In Eq. (19), the average (or fluid) ion quantities T_i, $\langle\mathbf{v}_i\rangle = \mathbf{V}_i$, $\langle\mathbf{v}_i\rangle^2$, and $\langle\mathbf{v}_i^2\rangle$ are derived at a grid point from interpolation of all particles in the surrounding cells using the fifth-order conservative weighting scheme. The average velocity of electrons at a grid point, $\langle\mathbf{v}_e\rangle = \mathbf{V}_e$, is obtained from the fluid model described above. The dynamic friction collision frequency in Eq. (19) can be calculated as

$$\nu_{ie} = \frac{8\sqrt{\pi} Z_i^2 e^4 n_e \ln\Lambda_{ie}}{m_{ie}^2 (\Delta v)^3}\left[\frac{\sqrt{\pi}}{2} erf\left(\frac{\Delta v}{v_{\rm th}}\right) - \frac{\Delta v}{v_{\rm th}}\exp\left(-\frac{\Delta v^2}{v_{\rm th}^2}\right)\right], \tag{20}$$

and the energy transfer collision frequency is given by

$$\nu_{ie}^\varepsilon = \frac{16\sqrt{\pi} Z_i^2 e^4 n_e \ln\Lambda_{ie}}{m_i m_e v_{\rm th}^3}\exp\left(-\frac{\Delta v^2}{v_{\rm th}^2}\right), \tag{21}$$

where $\Delta v = |\mathbf{V}_e - \mathbf{V}_i|$ and $v_{\rm th}^2 = 2k(T_i/m_i + T_e/m_e)$. After the Monte Carlo collision process has been completed, an ion particle with a velocity $\mathbf{v}_i$ is moved according to

$$\frac{d\mathbf{x}_i}{dt} = \mathbf{v}_i. \tag{22}$$

III. RESULTS AND DISCUSSION

A. Model validation

In this subsection, we validate the electron (fluid)–ion (particle) energy transfer calculation methods and hybrid fluid–PIC method with some test examples, before using the proposed model for actual simulations of physical systems. Here, we present two test examples for validation. The first example is a check of the energy transfer rate between fluid electrons and particle ions by setting the components of the plasma to have different temperatures. The electron fluid has a temperature of 0.1 keV, and the ions have an initial Maxwellian temperature $T_i = 10$ keV. The simulation is performed for a plasma with a uniform density $n_e = 10^{24}$ cm^{-3} and an ion mass $M = 1836 m_e$. The Coulomb logarithm $\ln\Lambda_{\alpha\beta}$ is determined by the Lee–More model. The simulation is performed in the x–y plane, with the plasma uniformly distributed in the simulation box, with 100×100 computational cells and 10^6 macroparticles. The time step is 0.6 fs. Both the particle and field boundary conditions are periodic, either in the x or the y direction. The self-consistent electromagnetic fields are turned on in the simulation so that the hybrid fluid–PIC scheme can also be verified. There is no relative drift, and the equilibration is described by[35]

$$\frac{dT_\alpha}{dt} = \sum_\beta \nu_\varepsilon^{\alpha\setminus\beta}(T_\beta - T_\alpha), \tag{23}$$

where

$$\nu_\varepsilon^{\alpha\setminus\beta} = 1.8\times10^{-19}\frac{(m_\alpha m_\beta)^{1/2} Z_\alpha^2 Z_\beta^2 n_\beta \ln\Lambda_{\alpha\beta}}{(m_\alpha T_\beta + m_\beta T_\alpha)^{3/2}}\ \text{s}^{-1}. \tag{24}$$

Here, α and β are the labels of the particle species inside the plasma. Equations (23) and (24) can be solved numerically.

Figure 1 shows the energy transfer between fluid electrons and particle ions. The simulation agrees well with the theoretical prediction of Eqs. (23) and (24) over the whole range of time evolution. We note that the internal ion–ion collisions are handled by the binary collision Monte Carlo method, and the energy transfer between fluid

electrons and particle ions is handled by the collision force from Eq. (19). It is important to stress that the plasma density in this test example is high enough to damp the plasma waves, and the physics is dominated by collisional processes. Hence, the electromagnetic field energy is negligible, and the system energy is dominated by the energy transfer between the fluid electrons and particle ions.

In the second test example, we consider two different species of ions (CH) with properties similar to those in the first example. In this case, we set the temperatures of both ion populations equal, $T_1 = T_2 = 10$ keV, and $T_e = 0.1$ keV for the electron fluid. The simulation is performed in the same geometry with the same number of cells but 2×10^6 particles. The ion number ratio is C:H = 1:1. Figure 2 shows the energy transfer between fluid electrons and the two ion species. Note that the temperature equilibration of the fluid electrons and the two ion species is again described by Eqs. (23) and (24). This test simulation also confirms that the energy transfer between fluid electrons and particle ions is handled correctly by our hybrid fluid–PIC code.

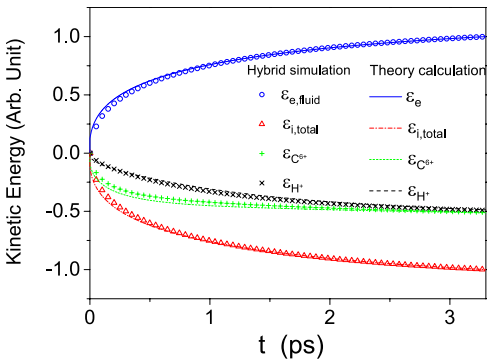

FIG. 2. Energy transfer between fluid electrons and two species of ions (C:H = 1:1) at density $n_e = 10^{24}$ cm^{-3}. The symbols indicate the simulation results, and the lines are calculated using Eq. (23). Here, all the energies are normalized by the maximum increment of the energy of the electron fluid at the end of the simulation time.

B. Hybrid fluid–PIC simulation of Richtmyer–Meshkov instability of a thermal interface

The problem of shock-driven hydrodynamic instabilities is crucial for understanding the detailed implosion physics in ICF. For instance, the Richtmyer–Meshkov instability (RMI)[38,39] exhibits complex late-time behavior, and it has been shown that this is related to the details of the initial interface. We now consider the evolution of shock-driven RMI[40] of perturbations at an interface separating two fluids. Here, an incident planar shock propagates from a light to a heavy plasma and then hits a single-mode sinusoidal perturbation surface. Here, a "light plasma" ("heavy plasma") is one in which the ion mass is low (high).

To elucidate kinetic effects on the RMI, we investigate a case where there is a jump in the initial density across the designed perturbed interface due to a discontinuity in ion species. The initial conditions are shown in Fig. 3. The initial configuration consists of two different plasmas: a hydrogen plasma ($Z = 1, A = 1, m_{i1} = 1836m_e$) and a carbon plasma ($Z = 1$, $A = 12$, $m_{i2} = 22\,032m_e$), separated by a sinusoidal perturbation surface with an amplitude-to-wavelength ratio $a/\lambda = 0.25$. The temperature of the electron fluid is 0.1 keV at the initial moment. The densities of the plasma species are $\rho_H = 0.08$ g/cm^3 in the left region and $\rho_C = 5.01$ g/cm^3 in the right region. The piston target is also hydrogen, with a density $\rho_d = 0.08$ g/cm^3 and a piston velocity $u_d = 3 \times 10^3$ μm/ns. The simulation box has 1000×100 computational cells and 1.6×10^6 macroparticles.

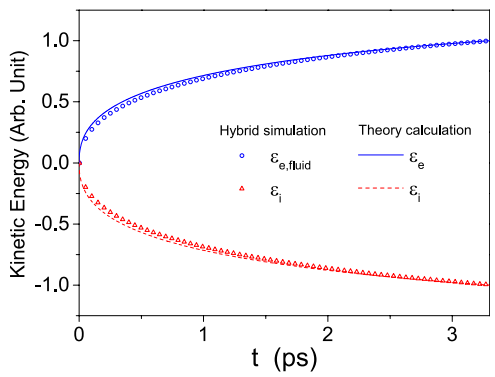

FIG. 1. Energy transfer between fluid electrons and particle ions of mass $M = 1836m_e$ at density $n_e = 10^{24}$ cm^{-3}. The circles and triangles indicate the simulation results, and the solid and dashed lines are calculated using Eq. (23). Here, all the energies are normalized by the maximum increment of the energy of the electron fluid at the end of the simulation time.

Figure 4 shows snapshots of the mass density of plasmas at $t = 2.02$, 4.04, 6.07, and 8.09 ps. As the shock wave hits the plasma interface, it splits into two nonplanar waves: a transmitted shock and a reflected shock. It then deposits baroclinic vorticity along the plasma interface, which results in characteristic rollups and ion mixing. The black contour near the interface in each panel of Fig. 4 encloses the region in which the fractions of both ion populations exceed 10%, and it thus reveals the growth of the ion mixing layer due to vorticity. This region encircled by the black contour is the so-called ion mixing region. In the growth of RMI, substantial ion mixing is introduced, which can enhance thermal energy loss and reduce the implosion performance in ICF. Note that ion mixing is self-consistently included in our simulations, which is the first merit of the hybrid fluid–PIC model. From Fig. 4, it can be seen that the growth of ion mixing is mainly due to vorticity rather than to increasing RMI amplitude $a(t)$. Here, the vorticity is baroclinically generated at the plasma interfaces in a continuous manner after the impact of the shock wave, which substantially enhances the growth of interface perturbations. The microstructural vortices can produce a wide mixing layer in a relatively short time. After that, the instability continues to develop at a reduced growth rate owing to the presence of the ion mixing layer. Note that when ion kinetic effects are taken into account, the instability can drive increased mixing and distortion of the transmitted shock, which may affect shock wave convergence in ICF implosions. At $t = 6.07$ ps, owing to the presence of a shear velocity between light and heavy plasmas, Kelvin–Helmholtz instability starts to grow on both sides of the interface. Figure 5 shows snapshots of the self-generated magnetic field B_z originating from Eq. (10) at $t = 2.02$, 4.04, 6.07, and 8.09 ps. However, in comparison with the electric field, the influence of the magnetic field on the ions is negligible, because the magnetic component of the Lorentz force is dependent on the ion

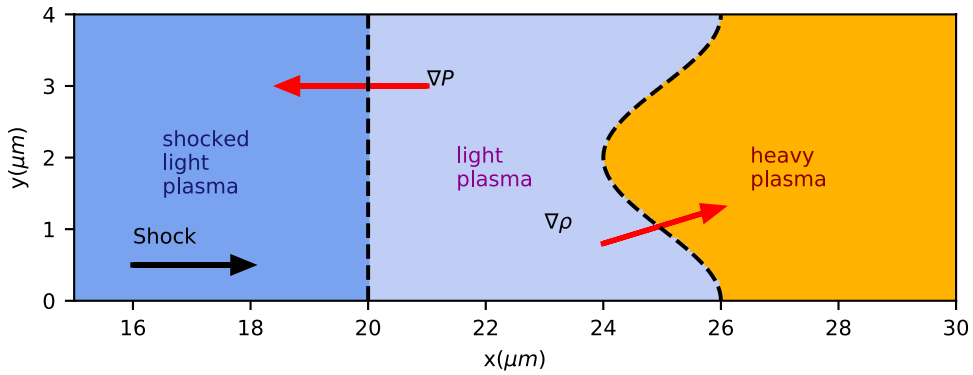

FIG. 3. Initial conditions for simulations of a piston-driven planar shock propagation through the perturbed interface separating two fluids of different densities.

velocity, which is much smaller than the velocity of light. The results obtained here provide significant insight into the microstructure of kinetic simulations of a shocked plasma, which can be used to determine the mechanism governing the growth of plasma instabilities, as well as to obtain better understanding of nonlinear ion mixing behavior.

C. Hybrid fluid–PIC simulation of Rayleigh–Taylor instability

We now consider ion kinetic effects on the growth of Rayleigh–Taylor instability (RTI)[41,42] using our hybrid fluid–PIC code. RTI occurs at an interface between two fluids of different densities during acceleration by a shock wave or a gravitational field. Here, the simulation is initialized with a step function plasma interface with initial perturbation peak-to-peak amplitude a_0. In particular, the gravitational field in the simulations is set to ensure that N e-foldings can be fulfilled during a simulation runtime $t_{\rm run}$ = 150 ps. Note that our hybrid fluid–PIC model does not have to resolve electron spatial scales as the standard PIC model does, which enables a long-runtime simulation. This is the second merit of the hybrid fluid-PIC model. The initial conditions are shown in Fig. 6(a). The initial configuration consists of two different plasmas: a heavy plasma (Z = 1, A = 12, m_{i1} = 22 032m_e) and a light plasma (Z = 1, A = 1, m_{i2} = 1836m_e), separated by a sinusoidal perturbation surface with an amplitude-to-wavelength ratio of a_0/λ = 0.25. As before, a light (heavy) plasma is one in which the ion mass is low (high). Note that in our simulation model, we set an initial density gradient tailored to match the gravitational field such that the system is in hydrostatic equilibrium, except for a cosine perturbation in density at the plasma interface. For simplicity, we set Z = 1 for both plasmas. The initial mass densities of the plasmas are ρ_L = 8.26 g/cm^3 (heavy plasma) in the left region and ρ_R = 0.69 g/cm^3 (light plasma) in the right region. In our simulation, the Atwood number A = 0.84 and gravity g = 7.2 × 10^{16} cm/s^2. The fluid electron temperature and the ion temperature are 0.1 keV throughout the volume. The simulation box has 1200 × 160 computational cells and 30 × 10^6 macroparticles.

The evolution of a single-mode heavy/light plasma interface shows the growth of RTI: see Figs. 6(b)–6(d). At the beginning, the heavy plasma forms a spike as it penetrates the light plasma. Later, at

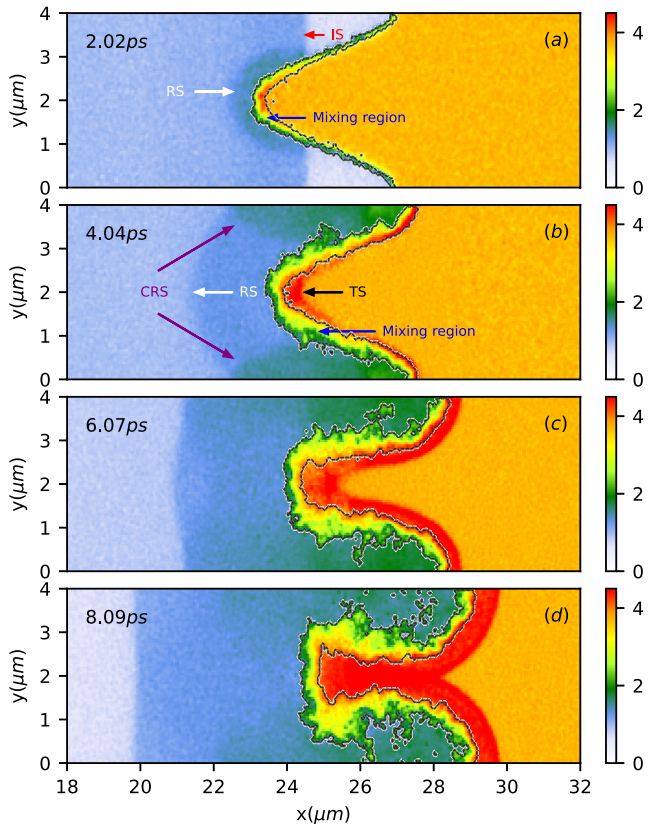

FIG. 4. Snapshots of the distribution of the logarithm of mass density (in units of g/cm^3) at times 2.02 ps (a), 4.04 ps (b), 6.07 ps (c), and 8.09 ps (d), showing the evolution of a single-mode hydrogen/carbon interface. IS denotes the incident shock, RS the reflected shock, TS the transmitted shock, and CRS the convergent reflected shock. As the incident shock wave passes through the plasma interface, it generates a slower second shock in the heavy plasma and a reflected shock running backward into the light plasma. The black contour near the interface encloses the region within which the fractions of both ion populations exceed 10%. This is the so-called ion mixing region.

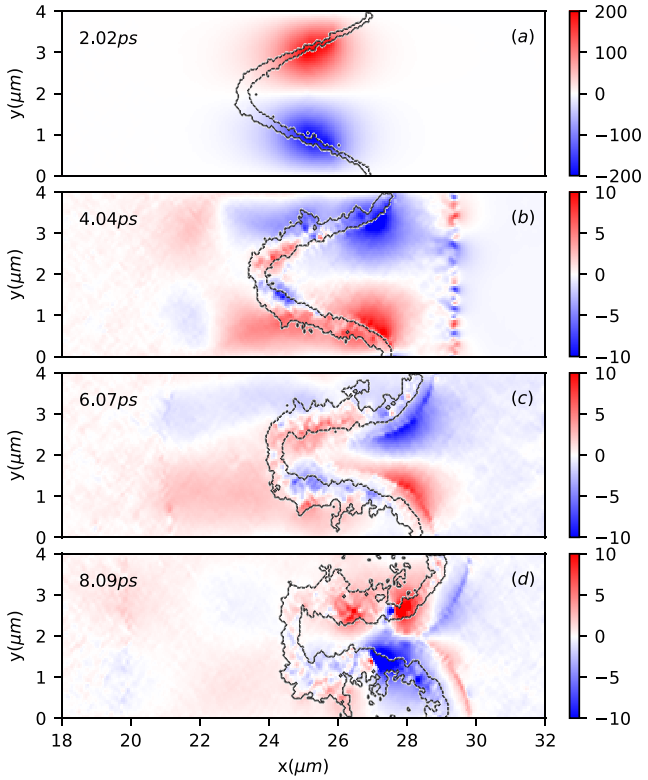

FIG. 5. Snapshots of self-generated magnetic fields B_z (in units of T) for RMI at times 2.02 ps (a), 4.04 ps (b), 6.07 ps (c), and 8.09 ps (d).

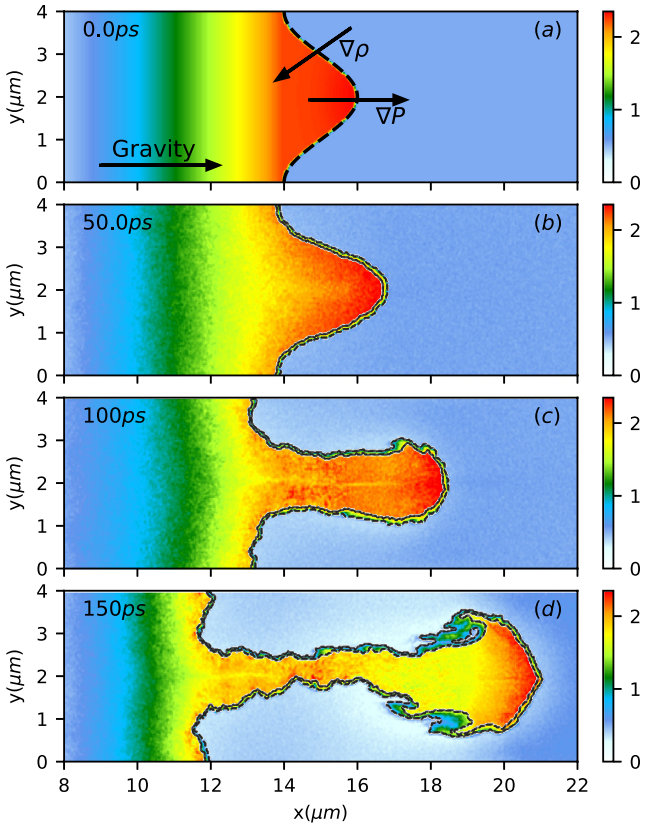

FIG. 6. (a) Initial conditions for simulation of ion kinetic effects on growth of Rayleigh–Taylor instability. (b)–(d) Snapshots of the distribution of the logarithm of mass density (in units of g/cm^3) at times 50 ps, 100 ps, and 150 ps, respectively, showing the evolution of a single-mode heavy/light plasma interface. The black contour near the interface encloses the region within which the fractions of both ion populations exceed 10% (the ion mixing region).

$t = 150$ ps, as the spike continues to grow, it rolls up at the tip owing to the growth of secondary Kelvin–Helmholtz instability. Compared with what is found in hydrodynamic simulations,[34] the secondary "mushroom cap" feature is weaker and secondary structures are suppressed in our hybrid simulation because of the ion mixing. It is important to mention that the evolution of RTI depends on the ion MFP in a plasma. According to our hybrid simulations, if the plasma density is high enough, ion mixing is insignificant because of the small ion MFP, and the RTI evolution and spike shape are then very similar to those in hydrodynamic simulations. On the contrary, if the plasma density is much lower, ion mixing will be more significant because of the larger ion MFP. In this case, the secondary structures will be completely suppressed by the ion mixing. We will consider the physics of this behavior in future work.

The self-consistently generated magnetic fields, which are mainly due to the Biermann battery effect $[\nabla \times (\nabla P_e/en_e) = -(k_B/e)(\nabla n_e \times \nabla T_e)/n_e$ in Eq. (10)], are depicted in Fig. 7 and have several interesting features. Compared with the Hall-MHD simulated magnetic fields presented by Srinivasan *et al.*,[43] our hybrid fluid–PIC simulated magnetic fields B_z have qualitatively the same profile in the linear phase of RTI, but with opposite magnetic direction. The physical reason is straightforward: in Ref. 43, the materials on both sides of the interface are the same deuterium plasma but with a hyperbolic tangent density profile and a hyperbolic cosine pressure profile across the interface (aligned with y) to satisfy $\nabla p \cdot \nabla \rho < 0$, and the electron density gradient along the direction of gravity (aligned with y) has $t\,(\nabla n_e)_g < 0$. By contrast, in our case, since the materials on each side of the interface are different, the electron density gradient along the direction of gravity (aligned with x) has $(\nabla n_e)_g > 0$ owing to the gravitational field and the evolution of RTI. Therefore, our hybrid-simulated magnetic fields have the opposite magnetic direction, since $\partial \mathbf{B}/\partial t \sim -\nabla n_e \times \nabla T_e$. Here, the magnetic energy is clearly smaller than the thermal and kinetic energies of the plasma. Hence, the magnetic fields cannot directly affect the growth of RTI. However, they can result in a significant electron thermal conductivity at the interface and intensify the formation of the spike. Note that the ability to study the influence of the self-generated electric and magnetic fields on the evolution of shock-driven hydrodynamic instabilities in a plasma is the third merit of our hybrid fluid–PIC model.

IV. SUMMARY

We have introduced a new hybrid fluid–PIC code for simulating the physics of shock waves and hydrodynamic instabilities in high-density plasmas. The massless electron fluid is described by the density continuity equation, electron pressure equation, and Ohm's law. The use of the density continuity equation and the retention of

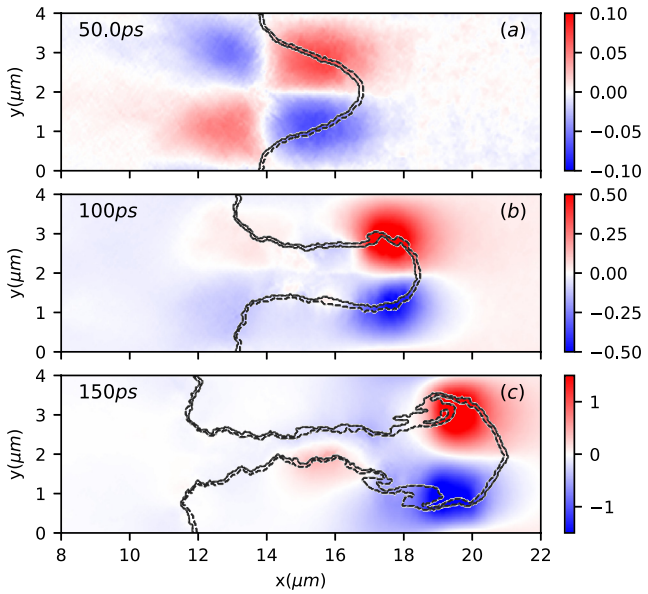

FIG. 7. Snapshots of the distribution of self-generated magnetic fields B_z (in units of T) for RTI at times 50 ps (a), 100 ps (b), and 150 ps (c).

the displacement current in Ampère's law ensure that charge conservation is satisfied and the charge separation electric field is simultaneously included throughout the simulation. Ion–ion collisions are modeled with a Monte Carlo method and ion–electron collisions by grid-based Coulomb collisions. This hybrid code allows us to model the microstructural physics of shock waves and hydrodynamic instabilities in high-density plasmas, taking account of ion kinetic effects, which would be a formidable task for a single-fluid code.

We have applied our hybrid fluid–PIC simulations to shock-driven RMI and RTI in high-density plasmas and have found that when ion kinetic effects are taken into account, the baroclinic vorticity along the plasma interface can result in significant ion mixing, which enhances thermal energy loss and reduces implosion performance in ICF. We have also found that although self-generated magnetic fields play a role in the generation of baroclinic vorticity along the interface and in late-time mixing of the plasmas, this is not enough to affect the instability itself directly. To the best of our knowledge, simulations of shock waves and hydrodynamic instabilities in the transition regime with $\lambda_{ii} \simeq L$, including the influence of ion kinetic effects on the shock convergence phase in ICF, have not yet been studied in detail. In the future, we hope to use our hybrid fluid–PIC code to address these topics.

ACKNOWLEDGMENTS

The authors thank Dr. Z. S. Dai, Dr. W. S. Zhang, Dr. B. Du, Dr. H. X. Huang, Dr. W. D. Zheng, Dr. E. H. Zhang, Dr. L. X. Li, Dr. H. Xu, Dr. D. Wu, Dr. P. Song, and Dr. S. Y. Zou for helpful discussions. This work was supported by the National Natural Science Foundation of China [Grant Nos. 11975055 and U1730449 (NSAF)] and the National Key Programme for S&T Research and Development (Grant No. 2016YFA0401100). The simulations were performed on the Tianhe-2 supercomputer (China).

REFERENCES

[1]O. A. Hurricane, D. A. Callahan, D. T. Casey, P. M. Celliers, C. Cerjan, E. L. Dewald, T. R. Dittrich, T. Döppner, D. E. Hinkel, L. F. Berzak Hopkins *et al.*, "Fuel gain exceeding unity in an inertially confined fusion implosion," Nature **506**, 343 (2014).

[2]V. A. Smalyuk, D. T. Casey, D. S. Clark, M. J. Edwards, S. W. Haan, A. Hamza, D. E. Hoover, W. W. Hsing, O. Hurricane, J. D. Kilkenny *et al.*, "First measurements of hydrodynamic instability growth in indirectly driven implosions at ignition-relevant conditions on the National Ignition Facility," Phys. Rev. Lett. **112**, 185003 (2014).

[3]J. P. Sauppe, S. Palaniyappan, E. N. Loomis, J. L. Kline, K. A. Flippo, and B. Srinivasan, "Using cylindrical implosions to investigate hydrodynamic instabilities in convergent geometry," Matter Radiat. Extremes **4**, 065403 (2019).

[4]T. Ma, P. K. Patel, N. Izumi, P. T. Springer, M. H. Key, L. J. Atherton, L. R. Benedetti, D. K. Bradley, D. A. Callahan, P. M. Celliers *et al.*, "Onset of hydrodynamic mix in high-velocity, highly compressed inertial confinement fusion implosions," Phys. Rev. Lett. **111**, 085004 (2013).

[5]V. A. Smalyuk, R. E. Tipton, J. E. Pino, D. T. Casey, G. P. Grim, B. A. Remington, D. P. Rowley, S. V. Weber, M. Barrios, L. R. Benedetti *et al.*, "Measurements of an ablator-gas atomic mix in indirectly driven implosions at the National Ignition Facility," Phys. Rev. Lett. **112**, 025002 (2014).

[6]M. J. Rosenberg, H. G. Rinderknecht, N. M. Hoffman, P. A. Amendt, S. Atzeni, A. B. Zylstra, C. K. Li, F. H. Séguin, H. Sio, M. Gatu Johnson *et al.*, "Exploration of the transition from the hydrodynamiclike to the strongly kinetic regime in shock-driven implosions," Phys. Rev. Lett. **112**, 185001 (2014).

[7]J. R. Rygg, J. A. Frenje, C. K. Li, F. H. Séguin, R. D. Petrasso, F. J. Marshall, J. A. Delettrez, J. P. Knauer, D. D. Meyerhofer, and C. Stoeckl, "Observations of the collapse of asymmetrically driven convergent shocks," Phys. Plasmas **15**, 034505 (2008).

[8]T. Gong, L. Hao, Z. C. Li, D. Yang, S. W. Li, X. Li *et al.*, "Recent research progress of laser plasma interactions in Shenguang laser facilities," Matter Radiat. Extremes **4**, 055202 (2019).

[9]H. G. Rinderknecht, P. A. Amendt, S. C. Wilks, and G. Collins, "Species separation in inertial confinement fusion fuels," Plasma Phys. Control. Fusion **60**, 064001 (2018).

[10]L. Q. Shan, H. B. Cai, W. S. Zhang, Q. Tang, F. Zhang, Z. F. Song, B. Bi, F. J. Ge, J. B. Chen, D. X. Liu *et al.*, "Experimental evidence of kinetic effects in indirect-drive inertial confinement fusion hohlraum," Phys. Rev. Lett. **120**, 195001 (2018).

[11]P.L. Yao, H.B. Cai, X.X. Yan, W.S. Zhang, B. Du, J.M. Tian *et al.*, "Kinetic study of transverse electron-scale interface instability in relativistic shear flows," Matter Radiat. Extremes **5**, 054403 (2020).

[12]V. A. Thomas and D. Winske, "Kinetic simulations of the Kelvin–Helmholtz instability at the magnetopause," J. Geophys. Res. **98**, 11425 (1993).

[13]J. A. Stamper, K. Papadopoulos, R. N. Sudan, S. O. Dean, E. A. McLean, and J. M. Dawson, "Spontaneous magnetic fields in laser-produced plasmas," Phys. Rev. Lett. **26**, 1012 (1971).

[14]R. Chodura, "A hybrid fluid-particle model of ion heating in high-Mach-number shock waves," Nucl. Fusion **15**, 55 (1975).

[15]C. Thoma, D. R. Welch, R. E. Clark, D. V. Rose, and I. E. Golovkin, "Hybrid-PIC modeling of laser-plasma interactions and hot electron generation in gold hohlraum walls," Phys. Plasmas **24**, 062707 (2017).

[16]A. G. Sgro and C. Nielson, "Hybrid model studies of ion dynamics and magnetic field diffusion during pinch implosions," Phys. Fluids **19**, 126 (1976).

[17]D. P. Higginson, P. Amendt, N. Meezan, W. Riedel, H. G. Rinderknecht, S. C. Wilks, and G. Zimmerman, "Hybrid particle-in-cell simulations of laser-driven plasma interpenetration, heating, and entrainment," Phys. Plasmas **26**, 112107 (2019).

[18]C. Bellei, H. Rinderknecht, A. Zylstra, M. Rosenberg, H. Sio, C. K. Li, R. Petrasso, S. C. Wilks, and P. A. Amendt, "Species separation and kinetic effects in collisional plasma shocks," Phys. Plasmas **21**, 056310 (2014).

[19]R. J. Mason, "Implicit moment PIC-hybrid simulation of collisional plasmas," J. Comput. Phys. **51**, 484 (1983).

[20]J. R. Davies, A. R. Bell, and M. Tatarakis, "Magnetic focusing and trapping of high-intensity laser-generated fast electrons at the rear of solid targets," Phys. Rev. E **59**, 6032 (1999).
[21]D. R. Welch, D. V. Rose, M. E. Cuneo, R. B. Campbell, and T. A. Mehlhorn, "Integrated simulation of the generation and transport of proton beams from laser-target interaction," Phys. Plasmas **13**, 063105 (2006).
[22]H. Xu, X. H. Yang, J. Liu, and M. Borghesi, "Control of fast electron propagation in foam target by high-Z doping," Plasma Phys. Control. Fusion **61**, 025010 (2019).
[23]D. Wu, W. Yu, Y. T. Zhao, D. H. H. Hoffmann, S. Fritzsche, and X. T. He, "Particle-in-cell simulation of transport and energy deposition of intense proton beams in solid-state materials," Phys. Rev. E **100**, 013208 (2019).
[24]J. J. Honrubia and J. Meyer-ter-Vehn, "Fast ignition of fusion targets by laser-driven electrons," Plasma Phys. Control Fusion **51**, 014008 (2009).
[25]B. I. Cohen, A. J. Kemp, and L. Divol, "Simulation of laser–plasma interactions and fast-electron transport in inhomogeneous plasma," J. Comput. Phys. **229**, 4591 (2010).
[26]F. Zhang, H. B. Cai, W. M. Zhou, Z. S. Dai, L. Q. Shan, H. Xu, J. B. Chen, F. J. Ge, Q. Tang, W. S. Zhang *et al.*, "Enhanced energy coupling for indirect-drive fast-ignition fusion targets," Nat. Phys. **16**, 810–815 (2020).
[27]B. Lembege and F. Simonet, "Hybrid and particle simulations of an interface expansion and of collisionless shock: A comparative and quantitative study," Phys. Plasmas **8**, 3967 (2001).
[28]H. B. Cai, S. Z. Wu, J. F. Wu, M. Chen, H. Zhang, M. Q. He, L. H. Cao, C. T. Zhou, S. P. Zhu, and X. T. He, "Review of the current status of fast ignition research at the IAPCM," High Power Laser Sci. Eng. **2**, 1 (2014).
[29]F. F. Chen, *Introduction to Plasma Physics and Controlled Fusion* (Springer, 1974), p. 166.
[30]S. I. Braginskii, "Transport processes in a plasma," in *Review of Plasma Physics I* (Consultants Bureau, New York, 1965).
[31]E. M. Epperlein and M. G. Haines, "Plasma transport coefficients in a magnetic field by direct numerical solution of the Fokker–Planck equation," Phys. Fluids **29**, 1029 (1986).
[32]Y. T. Lee and R. M. More, "An electron conductivity model for dense plasma," Phys. Fluids **27**, 1273 (1984).
[33]L. Spitzer and R. Härm, "Transport phenomena in a completely ionized gas," Phys. Rev. **89**, 977 (1953); L. Spitzer, *Physics of Fully Ionized Gases*, 2nd ed. (Interscience, New York, 1962).
[34]D. Bond, V. Wheatley, R. Samtaney, and D. I. Pullin, "Richtmyer–Meshkov instability of a thermal interface in a two-fluid plasma," J. Fluid Mech. **833**, 332 (2017).
[35]J. D. Huba, "NRL: Plasma formulary," Technical Report No. 16-1231-1005, Naval Research LABPhysics Branch, Washington DC, Beam, 2004.
[36]T. Takizuka and H. Abe, "A binary collision model for plasma simulation with a particle code," J. Comput. Phys. **25**, 205 (1997).
[37]M. E. Jones, D. S. Lemons, R. J. Mason, V. A. Thomas, and D. Winske, "A grid-based Coulomb collision model for PIC codes," J. Comput. Phys. **123**, 169–181 (1996).
[38]R. D. Richtmyer, "Taylor instability in shock acceleration of compressible fluids," Commun. Pure Appl. Math. **13**, 297 (1960).
[39]E. E. Meshkov, "Instability of the interface of two gases accelerated by a shock wave," Fluid Dyn. **4**, 101 (1969).
[40]B. Guan, Z. G. Zhai, T. Si, X. Y. Lu, and X. S. Luo, "Manipulation of three-dimensional Richtmyer–Meshkov instability by initial interfacial principal curvatures," Phys. Fluids **29**, 032106 (2017).
[41]G. Taylor, "The instability of liquid surfaces when accelerated in a direction perpendicular to their planes. I," Proc. R. Soc. London, Ser. A **201**, 192 (1950); Lord Rayleigh, "Investigation of the character of the equilibrium of an incompressible heavy fluid of variable density," Proc. London Math. Soc. **s1-14**, 170 (1882).
[42]B. A. Remington, H.-S. Park, D. T. Casey, R. M. Cavallo, D. S. Clark, C. M. Huntington, C. C. Kuranz, A. R. Miles, S. R. Nagel *et al.*, "Rayleigh–Taylor instabilities in high-energy density settings on the National Ignition Facility," Proc. Natl. Acad. Sci. U. S. A. **116**, 18233 (2018).
[43]B. Srinivasan, G. Dimonte, and X. Z. Tang, "Magnetic field generation in Rayleigh–Taylor unstable inertial confinement fusion plasmas," Phys. Rev. Lett. **108**, 165002 (2012).